NANO LETTERS
Letter
Cite This: Nano Lett. 2019, 19, 850−856
pubs.acs.org/NanoLett

Nanoscale Modulation of Friction and Triboelectrification via Surface Nanotexturing

Qiang Li,[†] In Ho Cho,[‡] Rana Biswas,[†,§,∥,⊥] and Jaeyoun Kim*[,†,⊥]

[†]Department of Electrical and Computer Engineering, [‡]Department of Civil, Construction, and Environmental Engineering, [§]Department of Physics and Astronomy, [∥]Ames Laboratory, and [⊥]Microelectronics Research Center, Iowa State University, Ames, Iowa 50011, United States

Supporting Information

ABSTRACT: Nanoscale contact electrification (CE) of elastomer surfaces and the resulting tribocharge formation are important in many branches of nanotechnology but their mechanism is not fully clarified. In this Letter, we investigate the mechanism using the recently discovered phenomenon of replica molding-induced nanoscale CE. By generating tribocharge distributions patterned in close correlation with the interfacial nanotextures, the phenomenon provides well-defined targets for the investigation. By applying a variety of scanning probe microscopy techniques (AFM/KPFM/EFM) and finite element modeling (FEM) to the tribocharge distributions, we extract a process model that can explain how their patterns are formed and affected by the interfacial nanotexture's morphology. It turns out that the cumulative distance of the elastomer's tangential sliding during the interfacial separation plays the key role in shaping the tribocharge's distribution pattern. The model proves remarkably universal, staying valid to nanotextures all the way down in the sub-10 nm regime. This replica molding-induced CE also turns out to be an effective tool for sculpting nanoscale tribocharge distributions into unconventional forms, such as rings, partial eclipses, and dumbbells. Both the model and the technique will prove useful in many areas of nanotechnology.

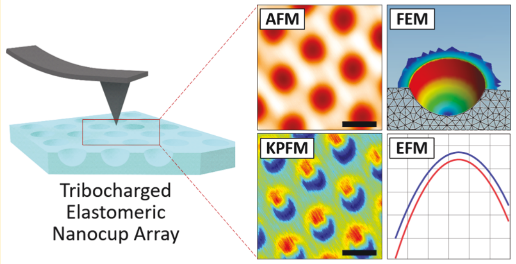

KEYWORDS: *Tribocharging, triboelectricity, contact electrification, Kelvin probe force microscopy, electrostatic force microscopy*

Generation of nanopatterned surface charge is important in many branches of nanotechnology, such as nanoxerography[1−4] and data storage.[5,6] Recently, contact electrification (CE)[7] is gaining popularity as a simple means to realize it. Of special interest is the CE induced by stamping nanotextured poly(dimethylsiloxane) (PDMS) masters onto the target surface because it can facilely achieve high-fidelity charge generation[8] and nanopatterning[9−11] thanks to the excellent flexibility of PDMS.

Further improving the nanoscale elastomeric CE requires understanding of its physical mechanism. In general, CE is attributed to the interfacial friction during the separation and the resulting generation of triboelectric charge.[12−19] However, the detailed process relating the two on elastomeric nanotextures is still elusive, despite significant advances in Kelvin probe force microscopy (KPFM)[20−22] and nanoscale charge characterization techniques based on it.[14,23−27]

In our recent work,[28] we observed an interesting phenomenon which may be useful to the study of the detailed process. While replicating nanotextured molds with PDMS (Figure 1a), we found that the demolding action (Figure 1b) induced tribocharges on the PDMS surface in a pattern closely correlated with the nanotexture. For example, the PDMS nanocups demolded from nanocones in our previous work exhibited ring-charges around their rims (Figure 1c). This replica molding-induced CE is a special case of the elastomeric CE and is capable of providing much more specific targets for further modeling and analysis.

On the basis that such a charge nanopatterning was not observed in the CE between flat surfaces,[23,29] we hypothesized that the mold's nanotexture has caused it during the demolding action, first by modulating the otherwise uniform friction into a nanopatterned friction, then by converting it into a similarly distributed tribocharge. To verify the hypothesis, we numerically simulated the demolding action (Figure 1d) and computed the friction pattern (Figure 1e). Its ring shape agreed excellently with the experimentally observed ring-charge pattern, successfully verifying the hypothesis.

Before generalizing these observations into a mechanotriboelectric model for the nanoscale elastomeric CE's mechanism, the following questions must be answered: Will different nanotextures lead to different friction patterns? Will such complex friction patterns still translate faithfully into congruent tribocharge distributions, as the simpler patterns did? Can a key factor governing the process be identified? Our previous work, focused mainly on the nanofabrication application of the phenomenon, experimented with only one nanotexture, leaving these questions unanswered.

Received: October 8, 2018
Revised: December 12, 2018
Published: January 14, 2019

DOI: 10.1021/acs.nanolett.8b04038
Nano Lett. 2019, 19, 850−856

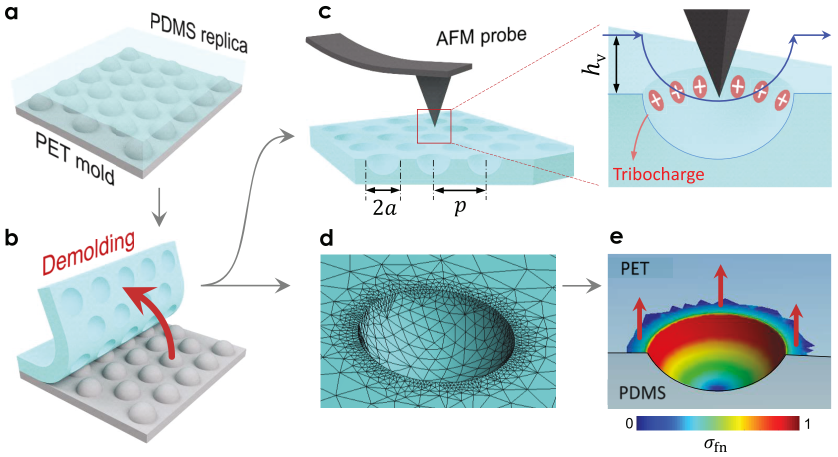

Figure 1. (a) A nanocone-textured PET mold is replicated with PDMS. (b) Demolding of the PDMS replica tribocharges the PDMS surface. (c) The PDMS surface is characterized by AFM, KPFM, and EFM. The blue curve indicates the tip's scanning path during KPFM and EFM. *a*, *p*, and h_v represent the nanocup's aperture radius, center-to-center spacing, and the tip−surface separation which in our setup are 250, 750, and 100 nm, respectively. The nanocup's depth *h* was varied. (d) The setup for finite element analysis of the demolding action. (e) The computed distribution of the normalized frictional stress σ_{fn} on a PDMS nanocup (h = 153 nm). The red arrows indicate the direction of replica/mold separation.

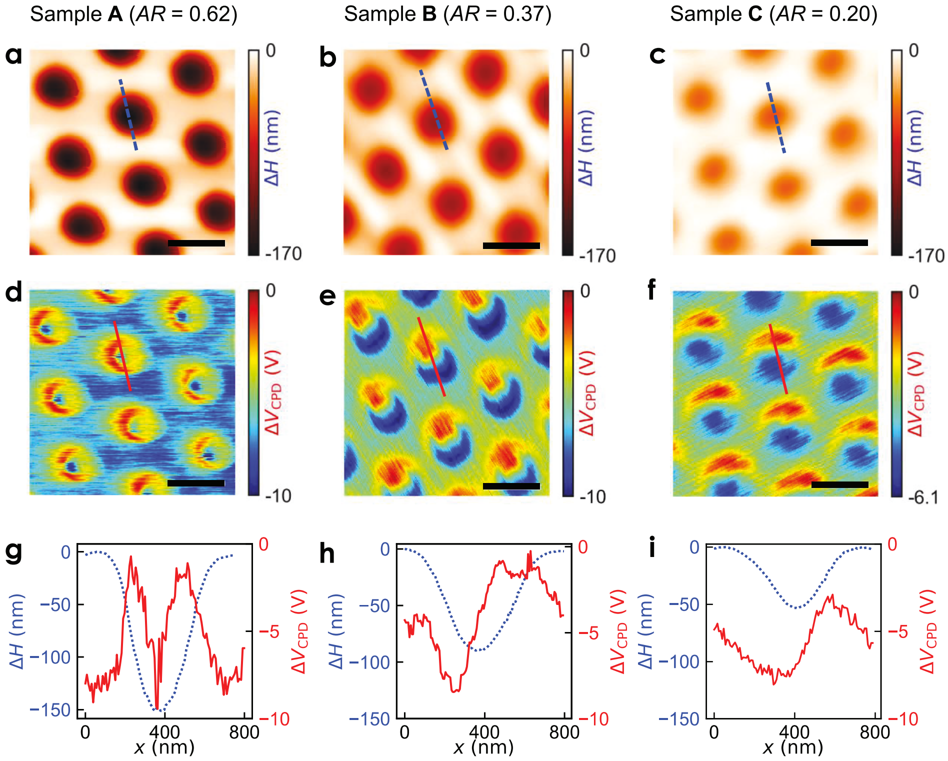

Figure 2. AFM surface topography (a−c) and the corresponding surface potential maps (d−f) of the samples **A** (AR = 0.62), **B** (AR = 0.37), and **C** (AR = 0.20), respectively. (g−i) The topographic and potential scans obtained along the blue dashed lines in (a−c) and the solid red lines in (d−f), respectively, are superimposed for facile correlation. (Scale bars: 500 nm.)

In this work, we attempt to answer the questions and clarify the mechanism using a greatly diversified set of interfacial nanotextures. Specifically, we vary the nanocone's aspect ratio which controls the direction and strength of the demolding force at submicron length-scales. We also reinforce the KPFM with electrostatic force microscopy (EFM)[30−34] for a more quantitative characterization of the charge. A three-dimensional (3D) computational model is developed as well to simulate the demolding action more realistically.

Using these new elements, we answer all three questions affirmatively. The outcome is two-fold. First, it leads to a mechano-triboelectric process model for the nanoscale elastomeric CE. The model turns out to remain valid to nanotextures all the way down in the sub-10 nm regime. Second, it also provides a highly scalable technique to create unconventional, complex charge nanopatterns as evidenced by the variety of the charge nanopatterns demonstrated in this work, such as rings, partial eclipses, and dumbbells. The mold material-dependence of the tribocharge's polarity is also observed.

The replica molding-induced CE process is summarized in Figure 1a,b. As the master mold, we adopted poly(ethylene terephthalate) (PET) plates (Microcontinuum Inc.) nanotextured with three different types of triangular nanocone arrays. No surface modification, physical or chemical, was performed to the master mold. Figure 1c shows the basic geometry of the PDMS nanocups demolded from the PET nanocones. The radius *a* and center-to-center spacing *p* of the nanocone were fixed at 250 and 750 nm, respectively. The nanocone's height (hence the nanocup's depth) *h* was varied to be 154.3 ± 7.8 nm (sample **A**), 93.5 ± 8.5 nm (sample **B**), and 50.2 ± 1.1 nm (sample **C**). The corresponding aspect ratios ($AR \equiv h/a$) were 0.62, 0.37, and, 0.20, respectively. Upon demolding, we probed the nanocups by atomic force microscopy (AFM) and KPFM (Figure 1c) to study the nanotexture's impact on the friction and charge distribution (for more details, see Supporting Information).

As the first target of KPFM, we chose sample **A** because its form-factor, especially the aspect ratio, is almost identical to those used in our previous work (*a*, *p*, and *h* at 250, 750, and 153 nm, respectively[28]). The only difference is that our previous nanocups were molded from nanocones made of polycarbonate (PC) which has lower charge-affinity than PET.[35]

The aspect ratio plays a critical role in the elastomeric CE process by strongly influencing the characteristics of the demolding force. In our previous work, we conjectured that at an aspect ratio as high as 0.62, the nanocup/nanocone separation must occur along the surface-normal direction, as shown in Figure 1e. Accordingly, we considered only the vertical lifting motion in the numerical simulation of the demolding action. Its result verified our conjecture by showing that such a vertical demolding motion indeed produces a ring-shaped friction pattern (the red strip in Figure 1e), which agrees excellently with the experimentally observed ring-charge pattern as shown schematically in Figure 1c. To reaffirm our conjecture of nanotexture-controlled demolding action, this ring-shaped friction needs to be reproduced by master molds with a similar shape and aspect ratio but made of different materials, such as the PET-based sample **A**.

Figure 2a,d show sample **A**'s topography and surface potential, respectively. Their cross-sectional profiles, obtained along the dotted and solid lines in Figure 2a,d, respectively, are superimposed in Figure 2g for facile correlation. Aside from a slight azimuthal asymmetry, the potential pattern takes the form of a ring and is located primarily around the nanocup's rim. The similarity of these features to those in our previous work[28] successfully reaffirms our conjecture of nanotexture-dependent friction modulation. The only significant difference is the vertical flipping of the surface potential profile. Figure 2d shows that the ring-shaped potential we just obtained from the PET mold takes a "dip-in-the-peak" profile which is a signature trait of a positive ring-charge.[1] In our previous work based on PC master molds, however, we observed a "peak-in-the-well" potential profile.[28] It is inverse to the "dip-in-the-peak" profile and also a signature trait of the negative ring-charge. This suggested reversal of polarity will be reaffirmed later in this Letter through EFM. It indicates that the charge affinity of PDMS may lie between those of PC (−5 nC/J) and PET (−40 nC/J).[35]

With our basic conjecture on the aspect ratio's role in the nanoscale CE reaffirmed, we proceeded to investigate how the changes in the aspect ratio affect the nanoscale CE. We used samples **B** and **C** which exhibit increasingly lower aspect ratios of 0.37 and 0.20, respectively. The second and third columns of Figure 2 show the results. Comparison of the KPFM results, facilitated by their juxtaposition, reveals that the charge distribution pattern in each nanocup changes gradually yet significantly from the original ring-shape (AR = 0.62) to a partial eclipse (AR = 0.37) and a dumbbell (AR = 0.20) as the aspect ratio decreases. On the basis of these results, we answer the first question affirmatively. The nanotexture indeed controls the friction pattern through its shape. Note that the potential variation across the PDMS nanocups becomes lower as the aspect ratio decreases due most probably to the weaker frictional stress during the demolding action.

Note that the red-to-blue transitions in Figure 2d−f indicate the decrease in the surface potential level generated by the tribocharges but not necessarily reversals in their polarity. The highly insulating nature of PDMS and the substantial thickness of the PDMS nanocup array (>1 mm) made it impossible to directly determine the surface potential or the tribocharge's polarity in the absolute sense. This issue will be addressed in the later part of this Letter with the help of EFM.

Verifying that these complex charge patterns were also generated by the same nanotexture-dependent friction modulation process that we hypothesized for the ring-charge is equivalent to answering the second question affirmatively. To that end, we numerically simulated the nanocup/nanocone demolding action. The simulation model differed from that for sample **A** in imposing a lateral crack opening-type demolding initiated from one side. As shown in Figure 3a, the crack opens from the leading edge (LE) on the left and propagates to the trailing edge (TE) on the right until the replica becomes fully separated from the mold. This new mode of demolding was necessary because the low aspect ratio of the nanocone appears to allow tangential sliding of one surface against the other, in addition to the vertical lifting, during the demolding. It contrasts with the case of high aspect ratio nanocones, such as sample **A**, in which the demolding is carried out mainly through the vertical lifting due to the high resistance to the sliding. Figure 3b,c shows how the frictional stress evolved during the demolding of sample **C**, the one with the lowest aspect ratio, from its PET mold. The inclusion of the lateral crack opening clearly concentrates the frictional stress on the TE side. The resulting breakdown of the reflectional symmetry within the nanocup agrees qualitatively with the experimentally observed asymmetry in Figure 2e,f.

The computed frictional stress patterns in Figure 3b,c, however, do not precisely match the features of the measured surface potential distribution shown in Figure 2f in detail. In particular, the sharp cusps in the TE area and the high contrast between the LE and TE areas clearly shown in Figure 2f are missing in Figure 3b,c, respectively. Such a mismatch is inevitable since the tribocharge's final distribution pattern is determined by the level of frictional stress accumulated throughout the demolding action at each point. Among many quantities that can be extracted from the simulation results, we found that the tangential sliding distance reflects the cumulative frictional stress most faithfully.

For facile comparison, we plotted the distribution of the tangential sliding distance, normalized to its maximum, in Figure 3d, and juxtaposed the normalized potential distribution, extracted from the KPFM scan of a single nanocup in sample **C**, as Figure 3e. They exhibit an improved level of similarity, especially in the salient features mentioned above, confirming the tangential sliding distance as the key factor that

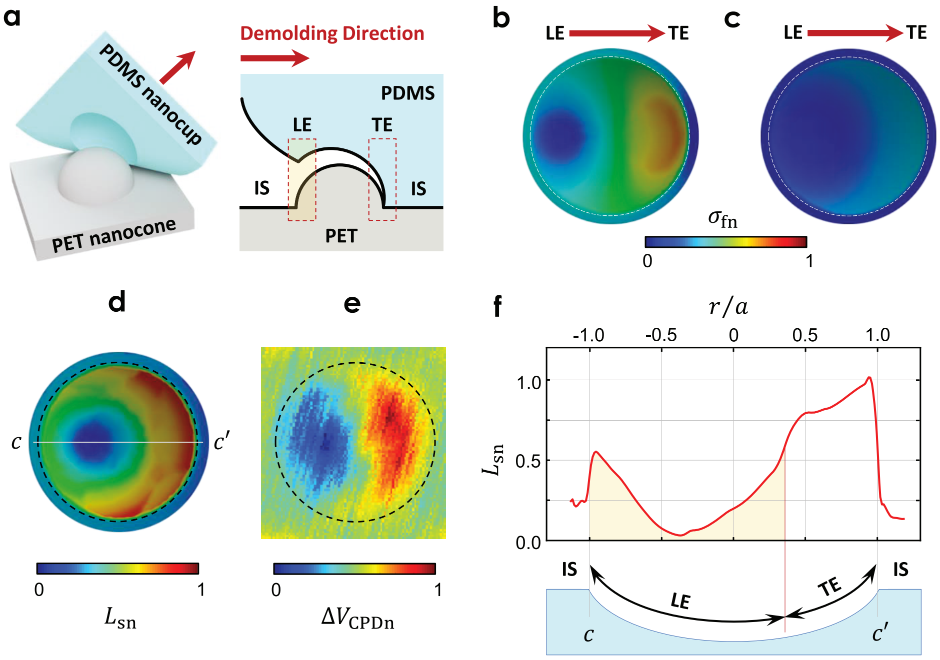

Figure 3. (a) Illustrations of the demolding action in bird's eye and cross-sectional views. The red arrows indicate the direction of demolding. LE, TE, and IS stand for the leading edge, trailing edge, and interstitial space, respectively. (b,c) The numerically computed distribution of the normalized frictional stress (σ_{fn}) at the initial and final stages of the demolding action in sample **C**, respectively. (d) Numerically computed distribution of the sliding distance (normalized to its maximum) due to the demolding action. (e) The normalized ΔV_{CPD} of one nanocup taken from Figure 2f. (f) The normalized sliding distance L_{sn} along the c−c' path in (d). It exhibits an asymmetric check mark-curve which resembles the KPFM scans in Figure 2h,i.

can be used to predict the charge distribution pattern in the nanoscale elastomeric CE.

To obtain more information, we extracted from the simulation result the normalized tangential sliding distance L_{sn} along the centerline c−c' in Figure 3d and plotted it in Figure 3f along with a schematic diagram of the PDMS nanocup. The plot reveals an asymmetric check mark (√)-shaped L_{sn} distribution inside a nanocup that can be qualitatively explained by our nanotexture-dependent friction modulation hypothesis: During the lateral crack opening-dominated demolding of low aspect ratio nanocones, the completely flat interstitial space (IS) outside the nanocup experiences a moderate, mostly uniform level of tangential sliding which forms the pedestal at $0.25 < L_{sn} < 0.5$ in Figure 3f. Once the demolding action reaches the leading edge of the nanocone, the replica and mold becomes separated rapidly, as illustrated schematically in Figure 3a, without involving much tangential sliding. In accordance, L_{sn} also drops rapidly from the IS-level, almost reaching zero at the center of LE, and then gradually increases as the crack opening approaches the peak of the nanocone and passes it. In contrast, TE experiences a significantly higher level of tangential sliding as the surfaces have to brush against each other during their separation. Consequently, L_{sn} not only recovers the IS level but also surpasses it, reaching the maximal level before returning to the IS level at the edge of the nanocup (Figure 3f).

If the nanotexture indeed modulated the friction in accordance with the model described above and the spatially modulated friction pattern were also faithfully converted into the tribocharge distribution, then we must be able to observe the check mark-shaped asymmetric L_{sn} distribution curve inside every low aspect ratio nanocup. Inspection of ΔV_{CPD} in Figures 2h and 2i verifies that it really is the case, enabling us to affirmatively answer not only the second question but also the third, by singling out L_{sn} as the factor governing the final charge distribution pattern.

To examine the range of validity of this nanotexture-controlled friction modulation and tribocharge patterning model, we set a sub-10 nm-scale nanotexture as our next target. The AFM scan in Figure 4a shows that ~4 nm-deep recesses appear at the midpoints of the triangular nanocup array's long diagonal. For the one in Figure 4b, the aspect ratio is only 0.027, which renders the region between the nanocup almost flat. We took KPFM scans along the dotted line in Figure 4a and plotted it in Figure 4c,d in superimposition with the surface topography.

Inside the two ~100 nm-deep nanocups, the potential changes exactly in agreement with the hypothesized model, exhibiting the characteristic check mark-curve between the intermediate pedestal level at $\Delta V_{CPD} \sim -4$ V. More remarkable is the appearance of a very similar check mark-curve inside the ~4 nm dip, as shown in magnified spatial scale in Figure 4d. It indicates that spatially varying CE can occur even at near-flat interfaces during their separation. Figure S1 shows that this nanoscale CE phenomenon is repeated in all the 16 shallow dips within a 3×3 μm^2 scan area. Applicability of the model to such a small and slowly varying nanotexture reinforces its validity, qualifying it as a full mechano-triboelectric model of the nanoscale elastomeric CE.

For completeness, we also tested the model's validity in a nanotexture with much greater vertical extent. We used a PET surface relief grating with its depth and pitch at 300 and 700 nm, respectively (Figure S2). Despite its depth, the large pitch ensured a smooth demolding as described in Figure 3a. The geometry's simplicity also rendered the control of the demolding direction easier and accurate, enabling us to

DOI: 10.1021/acs.nanolett.8b04038
Nano Lett. 2019, 19, 850−856

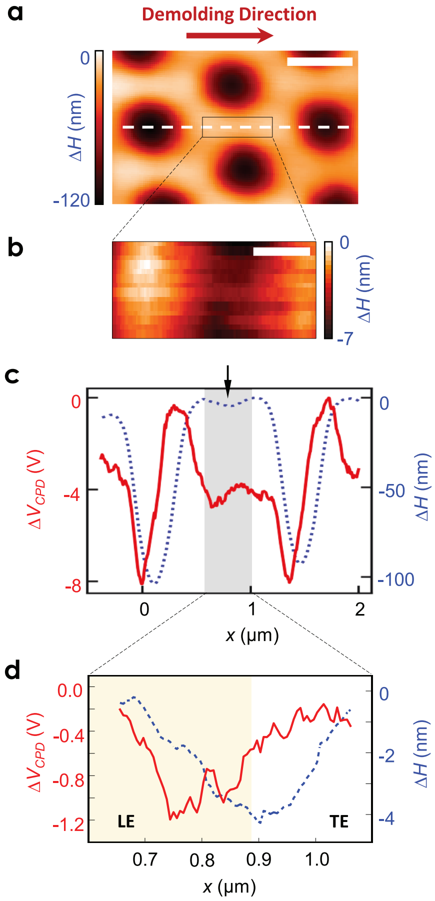

Figure 4. (a) Top-view topography of sample **B** nanocups (scale bar: 500 nm). (b) A sub-10 nm scale dip exists at the center of the interstitial area (scale bar: 150 nm). (c) AFM (dotted) and KPFM (solid) scans along the white dotted line in (a). The black down-arrow indicates the position of the sub-10 nm scale dip. (d) Magnified plots of ΔH and ΔV_{CPD} within the shaded region of (c).

deliberately reverse the direction and monitor its impact. The potential scans, superimposed with the topography for facile correlation (Figure S2c,f), clearly reveal the asymmetric check mark-curves with their minima near the mid-LE, reaffirming the validity of our model. Furthermore, they also reveal that the reversal of the demolding direction resulted in the matching left−right flipping of the check mark-curve, which further corroborates our model.

For a more quantitative validation of the mechano-triboelectric model, we refined the charge characterization technique. The issue is that PDMS is an insulator without a clearly defined Fermi level. Since KPFM relies its operation on the Fermi level difference, the electric potential measured on insulators becomes strongly affected by the sample preparation and/or the measurement setup,[36,37] making direct determination of the strength and polarity of the measured potential very difficult.[38] The relatively large thickness of the PDMS replica (>1 mm) aggravates the difficulty.[39] To address these issues, we adopted EFM which has been widely used for charge characterization on insulators such as epoxy resin,[30] nanocomposite,[31] and adatoms.[32] By tracking the electrostatic force generated by the surface charge, EFM can directly measure the charge's polarity and density even on highly insulating substrates,[33,34] complementing the results of KPFM.

In our setup, the sample substrate was grounded and we measured the resonance frequency shift Δf_0 of the cantilever probe as a function of the dc voltage V_{dc} applied to the probe. The frequency shift, proportional to the gradient of the force, is given by[30,33,40]

$$\frac{\Delta f_0}{f_0} \cong -\frac{1}{2k_c}\frac{\mathrm{d}F_{\mathrm{dc}}}{\mathrm{d}z} = -\frac{1}{2k_c}\frac{\mathrm{d}}{\mathrm{d}z}\left(\frac{1}{2}C'V_{\mathrm{dc}}^2 + \frac{q_s q_t}{4\pi\varepsilon_0 z^2}\right) \tag{1}$$

where f_0 is the resonance frequency of the probe, k_c is the cantilever spring constant, z is the vertical distance between the sample surface charge q_s and the image charge $q_t = -q_s + C\cdot V_{\mathrm{dc}}$ on the probe. F_{dc} is the force exerted on the probe, consisting of the capacitive contribution and the Columbic attraction, where C is the probe to substrate capacitance and C' the first derivative with respect to z.

Carrying out the differentiation in eq 1 reveals that the resonance frequency shift Δf_0 is quadratically related to V_{dc} as

$$\Delta f_0 = -\frac{f_0}{2k_c}\left(\frac{C''}{2}\cdot V_{\mathrm{dc}}^2 + \frac{q_s}{4\pi\varepsilon_0}\left(\frac{2C}{z^3} - \frac{C'}{z^2}\right)\cdot V_{\mathrm{dc}} - \frac{q_s^2}{2\pi\varepsilon_0 z^3}\right) \tag{2}$$

It is straightforward to show that the frequency shift Δf_0 maximizes at

$$V_{\mathrm{dc}}^* = \frac{q_s}{4\pi\varepsilon_0}\frac{1}{C''}\left(\frac{2C}{z^3} - \frac{C'}{z^2}\right) \tag{3}$$

With $\frac{1}{C''}\left(\frac{2C}{z^3} - \frac{C'}{z^2}\right)$ always positive, the polarity of the surface charge can be determined from the sign of V_{dc}^*. In addition, the surface charge q_s itself can be determined from the y-intercept as

$$|q_s| = \sqrt{\frac{4\pi\varepsilon_0 k_c h_v^3 |\Delta f_0(V_{\mathrm{dc}} = 0)|}{f_0}} \tag{4}$$

We conducted EFM on five PDMS nanocups in sample **C**. Figure 5a shows the resonance frequency shift at varying values of V_{dc}. We found that the topography images exhibited no significant variation other than slight shifts caused by the scanning drift (Figure S3a). In contrast, Δf_0 shifted considerably as a quadratic function of V_{dc}. Figure 5b shows the map obtained at $V_{\mathrm{dc}} = -10$ V in a magnified view. It is clear that the frequency shift within a single nanocup exhibits an asymmetric dumbbell pattern.

To quantify the difference in the surface charge, we plotted the frequency shifts in the left-hand and right-hand sides of nanocups as a function of the applied probe bias, as depicted in Figure 5c. The solid and dotted lines were the quadratic fitting to the data, with the maxima at 1.33 and 1.29 V in the left-hand side and right-hand side, respectively. The frequency shift at zero bias ($V_{\mathrm{dc}} = 0$) was measured to be −1.3 and −4.5 Hz.

From eqs 3 and 4, the surface charge was determined to be positive and the absolute value was 0.015 and 0.028 elementary charges per 10 nm^2. In the estimation, we assumed that the electrostatic coupling between the probe's tip and the surface occurred over an area of 10^4 nm^2, a typical value[30] which also is approximately the area of the blue circle in Figure 3d. From the subduplicate ratio between the Δf_0 values, it was estimated that the surface charge density in the right (TE) side was $\sqrt{4.5/1.3} \cong 1.86$ times higher than that in the left (LE) side. This difference in the charge density within a single nanocup is

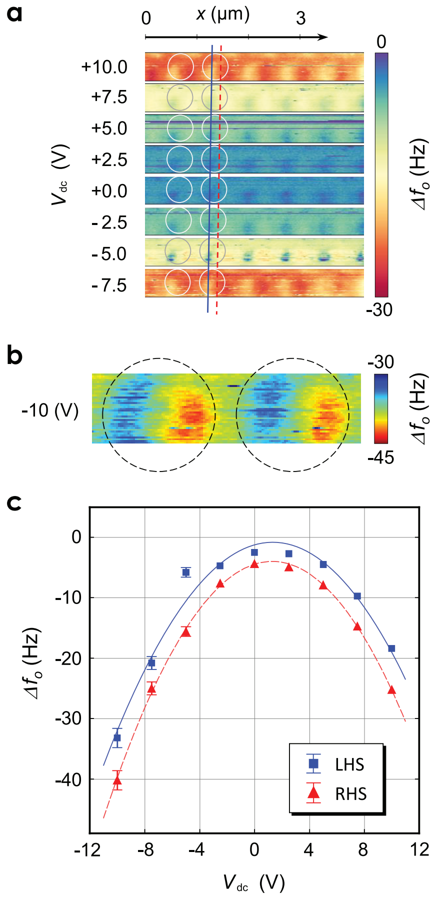

Figure 5. (a) EFM images of sample **C** under different values of V_{dc}. A row of five PDMS nanocups were probed for the shift in the resonance frequency Δf_0. (b) A magnified EFM image at $V_{dc} = -10$ V reveals the asymmetry in charge distribution. (Circle radius a = 250 nm.) (c) Δf_0 extracted from the left-hand side (LHS) and right-hand side (RHS) of the circled nanocup in (a) as a function of V_{dc}. The solid and dashed curves represent the parabolic curve fitting results. The error bars represent the standard deviation obtained from five samples. Error bars smaller than the symbols were omitted for visual clarity.

consistent with the surface potential patterns shown in Figure 2f. To quantitatively relate this tribocharge density ratio to the difference in the sliding distance experienced by the LE and TE areas, we integrated the areas under the LE (shaded) and TE (plain) portions of the normalized L_{sn} curve in Figure 3f. The ratio turns out to be approximately 1.98 which is very close to the charge density ratio obtained above. This result indicates that the sliding distance can be linearly related to the induced tribocharge density and corroborates the mechano-triboelectric model quantitatively.

In conclusion, we established a mechano-triboelectric model for the nanoscale elastomeric CE process by applying a variety of scanning probe microscopic techniques, for example, AFM, KPFM, and EFM, to the recently discovered phenomenon of replica molding-induced CE and correlating the results with a highly realistic computer simulation of the phenomenon. The adoption of the replica molding-induced CE was crucial to this study since its strong nanotexture-dependence provided well-defined targets for the characterization, modeling, and analysis. The resulting mechano-triboelectric process model showed that the surface nanotexture controls the tribocharge's distribution pattern by inducing spatially modulated friction during the demolding action. On the basis of the computer simulation results of the demolding action, we identified the tangential sliding distance as the key factor that can be used to predict the tribocharge's final distribution pattern. The model proves remarkably versatile with its prediction range covering all the way down to sub-10 nm scale surface textures with aspect-ratios as low as 0.027. The replica molding-induced CE process itself also proved very useful as a highly scalable technique to create unconventional, complex charge patterns, as evidenced by the partial eclipse- and dumbbell-shaped charge distributions shown above.

■ ASSOCIATED CONTENT

Ⓢ Supporting Information

The Supporting Information is available free of charge on the ACS Publications website at DOI: 10.1021/acs.nanolett.8b04038.

> Contact electrification via surface nanotexturing; Kelvin probe force microscopy and electrostatic force microscopy; finite element analysis: method, model, and interpretation; supporting figures (PDF)

■ AUTHOR INFORMATION

Corresponding Author

*E-mail: plasmon@iastate.edu.

ORCID

Qiang Li: 0000-0002-0701-8479
Rana Biswas: 0000-0002-0866-2100
Jaeyoun Kim: 0000-0003-4449-317X

Author Contributions

J.K. and R.B. conceived the idea and directed the study. Q.L. carried out most of the fabrication and experimental characterization work. I.C. performed the finite element analysis of the demolding action. The manuscript was written with contributions from all authors. All authors have given approval to the final version of the manuscript.

Funding

This work was supported by the National Science Foundation under Grants CMMI-1760348 (Q.L., J.K., R.B.) and also by Grants CMMI-1265844 (Q.L., J.K., R.B.) and CBET-1605275 (J.K., Q.L., and I.C., in part), the Department of Civil, Construction, and Environmental Engineering of Iowa State University (I.C., in part).

Notes

The authors declare no competing financial interest.

■ ACKNOWLEDGMENTS

We thank Microcontinuum Inc. for providing the nanocone array samples.

■ ABBREVIATIONS

CE, contact electrification; PDMS, poly(dimethylsiloxane); KPFM, Kelvin probe force microscopy; EFM, electrostatic force microscopy; PET, poly(ethylene terephthalate); AFM, atomic force microscopy; PC, polycarbonate; AR, aspect ratio; LE, leading edge; TE, trailing edge; IS, interstitial space; LHS, left-hand side; RHS, right-hand side

■ REFERENCES

(1) Jacobs, H. O.; Whitesides, G. M. Submicrometer Patterning of Charge in Thin-Film Electrets. *Science* **2001**, *291*, 1763−1766.

(2) Barry, C. R.; Gu, J.; Jacobs, H. O. Charging Process and Coulomb-Force-Directed Printing of Nanoparticles with Sub-100-nm Lateral Resolution. *Nano Lett.* **2005**, *5*, 2078−2084.

(3) Barry, C. R.; Jacobs, H. O. Fringing Field Directed Assembly of Nanomaterials. *Nano Lett.* **2006**, *6*, 2790−2796.

(4) Jacobs, H. O.; Campbell, S. A.; Steward, M. G. Approaching Nanoxerography: The Use of Electrostatic Forces to Position Nanoparticles with 100 nm Scale Resolution. *Adv. Mater.* **2002**, *14*, 1553−1557.

(5) Born, A.; Wiesendanger, R. Present and Future Developments of SPM Systems as Mass Storage Devices. *Appl. Phys. A: Mater. Sci. Process.* **1999**, *68*, 131−135.

(6) Kuang, S. Y.; Zhu, G.; Wang, Z. L. Triboelectrification-Enabled Self-Powered Data Storage. *Adv. Sci.* **2018**, *5*, 1700658.

(7) McCarty, L. S.; Whitesides, G. M. Electrostatic Charging Due to Separation of Ions at Interfaces: Contact Electrification of Ionic Electrets. *Angew. Chem., Int. Ed.* **2008**, *47*, 2188−2207.

(8) Dudem, B.; Huynh, N. D.; Kim, W.; Kim, D. H.; Hwang, H. J.; Choi, D.; Yu, J. S. Nanopillar-Array Architectured PDMS-Based Triboelectric Nanogenerator Integrated with a Windmill Model for Effective Wind Energy Harvesting. *Nano Energy* **2017**, *42*, 269−281.

(9) Cole, J. J.; Barry, C. R.; Wang, X.; Jacobs, H. O. Nanocontact Electrification through Forced Delamination of Dielectric Interfaces. *ACS Nano* **2010**, *4*, 7492−7498.

(10) Cole, J. J.; Barry, C. R.; Knuesel, R. J.; Wang, X.; Jacobs, H. O. Nanocontact Electrification: Patterned Surface Charges Affecting Adhesion, Transfer, and Printing. *Langmuir* **2011**, *27*, 7321−7329.

(11) Zhao, D.; Duan, L.; Xue, M.; Ni, W.; Cao, T. Patterning of Electrostatic Charge on Electrets Using Hot Microcontact Printing. *Angew. Chem., Int. Ed.* **2009**, *48*, 6699−6703.

(12) Collins, A. L.; Camara, C. G.; Naranjo, B. B.; Putterman, S. J.; Hird, J. R. Charge Localization on a Polymer Surface Measured by Triboelectrically Induced X-Ray Emission. *Phys. Rev. B: Condens. Matter Mater. Phys.* **2013**, *88*, 064202.

(13) Williams, M. W. Triboelectric Charging of Insulating Polymers-Some New Perspectives. *AIP Adv.* **2012**, *2*, 010701.

(14) Zhou, Y. S.; Liu, Y.; Zhu, G.; Lin, Z.; Pan, C.; Jing, Q.; Wang, Z. L. In Situ Quantitative Study of Nanoscale Triboelectrification and Patterning. *Nano Lett.* **2013**, *13*, 2771−2776.

(15) Collins, A. L.; Camara, C. G.; Van Cleve, E.; Putterman, S. J. Simultaneous Measurement of Triboelectrification and Triboluminescence of Crystalline Materials. *Rev. Sci. Instrum.* **2018**, *89*, 013901.

(16) Bhatia, D.; Kim, W.; Lee, S.; Kim, S. W.; Choi, D. Tandem Triboelectric Nanogenerators for Optimally Scavenging Mechanical Energy with Broadband Vibration Frequencies. *Nano Energy* **2017**, *33*, 515−521.

(17) Bhatia, D.; Lee, J.; Hwang, H. J.; Baik, J. M.; Kim, S.; Choi, D. Design of Mechanical Frequency Regulator for Predictable Uniform Power from Triboelectric Nanogenerators. *Adv. Energy Mater.* **2018**, *8*, 1702667.

(18) Xu, C.; Zi, Y.; Wang, A. C.; Zou, H.; Dai, Y.; He, X.; Wang, P.; Wang, Y. C.; Feng, P.; Li, D.; Wang, Z. L. On the Electron-Transfer Mechanism in the Contact-Electrification Effect. *Adv. Mater.* **2018**, *30*, 1706790.

(19) Xu, C.; Wang, A. C.; Zou, H.; Zhang, B.; Zhang, C.; Zi, Y.; Pan, L.; Wang, P.; Feng, P.; Lin, Z.; Wang, Z. L. Raising the Working Temperature of a Triboelectric Nanogenerator by Quenching Down Electron Thermionic Emission in Contact-Electrification. *Adv. Mater.* **2018**, *30*, 1803968.

(20) Jacobs, H. O.; Knapp, H. F.; Stemmer, A. Practical Aspects of Kelvin Probe Force Microscopy. *Rev. Sci. Instrum.* **1999**, *70*, 1756−1760.

(21) Melitz, W.; Shen, J.; Kummel, A. C.; Lee, S. Kelvin Probe Force Microscopy and Its Application. *Surf. Sci. Rep.* **2011**, *66*, 1−27.

(22) Girard, P.; Ramonda, M.; Saluel, D. Electrical Contrast Observations and Voltage Measurements by Kelvin Probe Force Gradient Microscopy. *J. Vac. Sci. Technol., B: Microelectron. Process. Phenom.* **2002**, *20*, 1348.

(23) Baytekin, H. T.; Patashinski, A. Z.; Branicki, M.; Baytekin, B.; Soh, S.; Grzybowski, B. A. The Mosaic of Surface Charge in Contact Electrification. *Science* **2011**, *333*, 308−312.

(24) Byun, K. E.; Cho, Y.; Seol, M.; Kim, S.; Kim, S. W.; Shin, H. J.; Park, S.; Hwang, S. Control of Triboelectrification by Engineering Surface Dipole and Surface Electronic State. *ACS Appl. Mater. Interfaces* **2016**, *8*, 18519−18525.

(25) Knorr, N. Squeezing out Hydrated Protons: Low-Frictional-Energy Triboelectric Insulator Charging on a Microscopic Scale. *AIP Adv.* **2011**, *1*, 022119.

(26) Zhou, Y. S.; Wang, S.; Yang, Y.; Zhu, G.; Niu, S.; Lin, Z. H.; Liu, Y.; Wang, Z. L. Manipulating Nanoscale Contact Electrification by an Applied Electric Field. *Nano Lett.* **2014**, *14*, 1567−1572.

(27) Galembeck, A.; Costa, C. A. R.; da Silva, M. C. V. M.; Souza, E. F.; Galembeck, F. Scanning Electric Potential Microscopy Imaging of Polymers: Electrical Charge Distribution in Dielectrics. *Polymer* **2001**, *42*, 4845−4851.

(28) Li, Q.; Peer, A.; Cho, I. H.; Biswas, R.; Kim, J. Replica Molding-Based Nanopatterning of Tribocharge on Elastomer with Application to Electrohydrodynamic Nanolithography. *Nat. Commun.* **2018**, *9*, 974.

(29) Bubendorfer, A. J.; Ingham, B.; Kennedy, J. V.; Arnold, W. M. Contamination of PDMS Microchannels by Lithographic Molds. *Lab Chip* **2013**, *13*, 4312−4316.

(30) El Khoury, D.; Arinero, R.; Laurentie, J. C.; Castellon, J. Nanoscale Surface Charge Detection in Epoxy Resin Materials Using Electrostatic Force Spectroscopy. *AIP Adv.* **2016**, *6*, 035318.

(31) Deschler, J.; Seiler, J.; Kindersberger, J. Detection of Charges at the Interphase of Polymeric Nanocomposites. *IEEE Trans. Dielectr. Electr. Insul.* **2017**, *24*, 1027−1037.

(32) Gross, L.; Mohn, F.; Liljeroth, P.; Repp, J.; Giessibl, F. J.; Meyer, G. Measuring the Charge State of an Adatom with Noncontact Atomic Force Microscopy. *Science* **2009**, *324*, 1428−1431.

(33) Portes, L.; Girard, P.; Arinero, R.; Ramonda, M. Force Gradient Detection under Vacuum on the Basis of a Double Pass Method. *Rev. Sci. Instrum.* **2006**, *77*, 096101.

(34) Riedel, C.; Arinero, R.; Tordjeman, P.; Ramonda, M.; Leveque, G.; Schwartz, G. A.; de Oteyza, D. G.; Alegria, A.; Colmenero, J. Determination of the Nanoscale Dielectric Constant by Means of a Double Pass Method Using Electrostatic Force Microscopy. *J. Appl. Phys.* **2009**, *106*, 024315.

(35) Jie, Y.; Wang, N.; Cao, X.; Xu, Y.; Li, T.; Zhang, X.; Wang, Z. L. Self-Powered Triboelectric Nanosensor with Poly-(Tetrafluoroethylene) Nanoparticle Arrays for Dopamine Detection. *ACS Nano* **2015**, *9*, 8376−8383.

(36) Barth, C.; Foster, A. S.; Henry, C. R.; Shluger, A. L. Recent Trends in Surface Characterization and Chemistry with High-Resolution Scanning Force Methods. *Adv. Mater.* **2011**, *23*, 477−501.

(37) Sadeghi, A.; Baratoff, A.; Ghasemi, S. A.; Goedecker, S.; Glatzel, T.; Kawai, S.; Meyer, E. Multiscale Approach for Simulations of Kelvin Probe Force Microscopy with Atomic Resolution. *Phys. Rev. B: Condens. Matter Mater. Phys.* **2012**, *86*, 075407.

(38) Neff, J. L.; Rahe, P. Insights into Kelvin Probe Force Microscopy Data of Insulator-Supported Molecules. *Phys. Rev. B: Condens. Matter Mater. Phys.* **2015**, *91*, 085424.

(39) Bocquet, F.; Nony, L.; Loppacher, C.; Glatzel, T. Analytical Approach to the Local Contact Potential Difference on (001) Ionic Surfaces: Implications for Kelvin Probe Force Microscopy. *Phys. Rev. B: Condens. Matter Mater. Phys.* **2008**, *78*, 035410.

(40) Terris, B. D.; Stern, J. E.; Rugar, D.; Mamin, H. J. Contact Electrification Using Force Microscopy. *Phys. Rev. Lett.* **1989**, *63*, 2669−2672.

DOI: 10.1021/acs.nanolett.8b04038
Nano Lett. 2019, 19, 850−856